Broadband Vibrational Energy Harvesting with a Spherical Piezoelectric Transducer Devoted to Underwater Wireless Sensor Networks

Daher Diab[1,3)], Nikolay Smagin[1)], Fabrice Lefebvre[1)], Georges Nassar[1)], Samih Isber[2)], Fawaz El Omar[3)], Adnan Naja[3)]

[1)] Univ. Polytech. Hauts-de-France, CNRS, Univ. Lille, ISEN, Centrale Lille, UMR 8520 - IEMN, DOAE, 59313 Valenciennes, France. daher_diab_90@hotmail.com

[2)] Department of Physics, American University of Beirut, Bliss Street, Riad el Solh, 1107 2020 Beirut, Lebanon

[3)] Laboratory of Physics and Modeling, EDST, Lebanese University, Tripoli, 1300 Lebanon

Summary

A new sensing node container based on a spherical piezoelectric transducer is proposed. This device provides broadband vibrational energy harvesting and sensing facilities intended for underwater wireless sensor networks. The transducer is composed of two acrylic glass (PMMA) half-spherical shells and a Pz26 piezoelectric ring clamped between the two shells. A simulation model of vibrational energy harvesting has been developed with electromechanical circuits for thickness and radial vibrational modes. This approach was validated by a finite element simulation. As a result, optimal power harvesting conditions and estimated harvested voltage were defined. A prototype of 2.2 cm in diameter was realized and characterized. Analysis in air environment reveals several structural resonance modes in the 20–80 kHz frequency range. The directivity patterns corresponding to these modes was obtained using laser Doppler vibrometry. The measurements for the underwater environment show that the structural resonance modes shift down in frequency to the 10–60 kHz range, and exhibiting low directivity dependence. Power harvesting performances was measured and quantified relative to acoustical pressure measurements using a hydrophone. The average conversion coefficient value was found to be in the order of 3 V/MPa. In broadband excitation mode, and for an acoustic pressure of 10 kPa, the amount of harvested power out of 5 main resonance modes is 3.3 μW.

PACS no. 43.40.At

1. Introduction

Recently, Underwater Wireless Sensor Networks (UWSNs) [1, 2, 3] as a part of the general Wireless Sensor Networks (WSNs) concept [4, 5] have attracted substantial attention due to their promising applications in monitoring, tracking and detection in shallow water as well as in deep oceans [6, 7, 8, 9]. Electromagnetic radio frequency and optical waves demonstrate low efficiency in underwater applications because of high attenuation and scattering in aqueous media. On the other hand, acoustical waves provide sufficient performances in propagation distance and emitting/receiving antennas [10, 11].

In order to provide a sustainable UWSN operation, the problem of autonomous and permanent energy supply for low-power electronics of sensing nodes should be solved [12]. For underwater applications, electric batteries are not preferable due to low accessibility of the sensing nodes for battery replacement and the danger that batteries present

to aqueous ecosystems. In this context, energy harvesters converting ambient energy into electrical energy are considered as a promising solution for a long-term energy supply [13].

Ocean contains large quantities of acoustic energy exploitable for electronics power supply, such as, ultrasonic waves generated in the ocean either naturally by animals, geological activity or artificially by antennas for underwater detection, navigation and communication [14, 15]. One of the fascinating points is that underwater ambient acoustic noise can be used for medium parameters monitoring and positioning [16] simultaneously with the energy supply function. Nevertheless, underwater ultrasonic energy harvesting is challenging due to efficiency issues in coupling of acoustic waves with energy harvesting device, as well as elevated requirements for durability and packaging [17, 18].

Vibration energy conversion mechanisms generally used for energy harvesting are electromagnetic [19], electrostatic [20], piezoelectric [21, 22]. Among these, the piezoelectric energy harvesting has an advantage of high power density, wide property range and ease of applica-

tion [23, 24]. Common harvester configurations are based on mass-loaded cantilever beams [21] as well as pressure-loaded plates or membranes [25]. A promising approach is to use custom-shaped (generally, cylindrical or spherical) shells completely made of a piezoelectric material or of a sandwich structure containing such a material [26]. Up to date, most of the results on shell-type piezoelectric transducers were obtained by analytical and numerical modeling with few experimental implementations. Kim *et al.*developed a model for a clamped circular monomorph piezoelectric plate (of radius a), they investigated the influence of thickness and pattern of the layer on the effect of energy conversion and harvesting. They found out that an optimal pattern for clamped circular monomorph under uniform pressure loading is obtained by reversing the polartity in the piezoelectric layer beyond $(\sqrt{2}/2)a$, they have also suggested that the patterned polarization concept may be useful in other structures [27]. This approach is promising but it could be challenging to implement due to issues with fabrication of the shell.

More recently, the acoustic metamaterials have been found to possess appropriate abilities for the energy harvesting applications, Gonella el al. proposed a multifunctional periodical structure design to absorb elastic waves within specific frequency ranges. They investigated a new structure for energy harvesting based on a regular hexagonal honeycomb embedded with piezoelectric microstructure. They proposed a new type of device relying on internal mechanisms rather than the conventional devices exploiting the direct interaction of the piezoelectric material with external vibrations [28]. While conventional energy harvesters are usually based on the structural resonance phenomena, metamaterials have a unique ability to concentrate energy inside the device due to the local resonance phenomena [23, 29]. This ability could be used to scale down energy harvesters because of operation in subwave length mode [30]. Energy harvesting with metamaterials is an emerging field now and it is supposed to become an efficient alternative to conventional devices.

Most studies have considered harvesting devices designated for functioning in conjunction with the ambient excitation at a given frequency [23, 31]. In general, such devices are designed using cantilever beams which provide a resonance-based energy harvesting [21, 32]. Resonance harvesters have to be pre-tuned to the external excitation but it is also possible to design a self-tuning device [33, 34]. However, in many applications, the ambient energy is random and broadband, and the energy harvester must be adapted for these conditions.

The purpose of this work is to develop an efficient, wideband and low- cost piezoelectrical energy harvester and sensing node container for UWSNs. We designed a spherical outer shell as a resonator and a clamped PZT ring as an energy converter. Our proposed configuration allows operating in a wide frequency range because of 5 principal structural resonating modes distributed in a rather narrow frequency rang (10–60 kHz). Our measurements showed a low directivity dependence which is quite favorable for
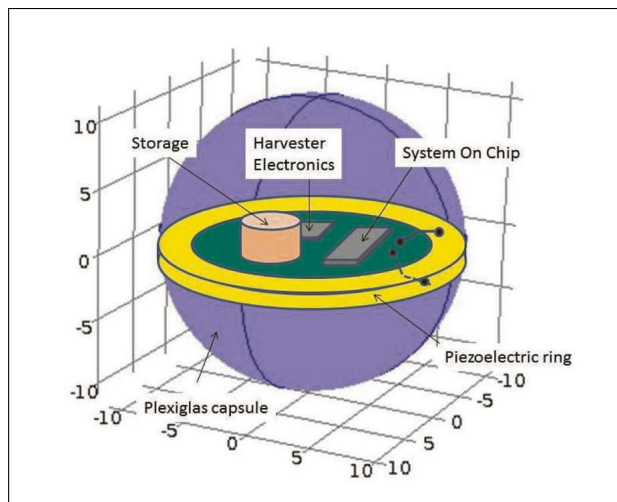

Figure 1. Concept of a spherical sensor where the hollow portion of the sphere contains embedded electronics.

operation in random ambient conditions. To the best of our knowledge, this is the first realization of a spherical multi-frequency structural resonator for UWSN applications.

The outer sensor shell is assembled out of two half-spheres acrylic glass (PMMA) with 10 mm inner radius and 1 mm thickness as shown in Figure 1. The piezoelectric ring (PZT-Pz26, 1 mm of thickness) is clamped between the two half-spheres. In comparison to shell devices [26], a PZT ring-based device is simpler to fabricate. In addition, two half-spheres configuration gives a possiblity to easily design a self-containing device, which can enclose all energy harvesting and communication electronics and has an inherent water pressure resistance and floater abilities allowing maintaining sensor position in aqueous media.

Conventionally, bandwidth widening can be achieved using a generator array (or multi-cell approach), a mechanical stopper, nonlinear (e.g. magnetic) springs or bistable structures [34]. Wideband solutions have been also proposed by several authors based on stack piezoelectric transducer configuration [31]. From a methodological point of view, our study is similar to that of Ahmed *et al.* [30] where multi-frequency approach has been employed for the case of a sonic crystal consisting of a spherical core encapsulated inside an elastic matrix, but in the experimental study, only one particular resonating mode has been chosen.

Furthermore, in this work, the optimal load impedance was determined by analytical modeling taking into account the various mode of vibrations. The simulation model of the piezoelectric ring has been developed considering two natural modes of vibration: the thickness mode and the radial one. For each mode, the ring behavior was simulated by an equivalent electromechanical circuit connecting the mechanical ports (forces and velocities) to the electrical port (voltage and current). It was found that the radial mode is predominant in power generation, and thus, it was used to calculate the optimal load impedance (25 kΩ).

To validate the electromechanical circuit model, a Finite Element Method (FEM) simulation was employed. The results of FEM modeling allowed us to estimate scavenged voltage for the first two resonating frequencies. Finally, experimental measurements of Electrical Impedance Analyzer (EIA) combined with Laser Doppler Vibrometer (LDV) allowed us to identify the first five resonating modes in air environment. All resonance frequencies for the five modes were found to be in the 10–100 kHz range. Furthermore, harvesting performance of the spherical shell in water was also studied, we measured the resonance frequencies shift, directivity patterns and generated power. The performance of energy conversion of the spherical shell in water was estimated to be ($\sim$3 V/MPa) and an output power ranging from $\sim$0.15 µW to $\sim$2.5 µW.

2. Analytical Model Of Piezoelectric Ring

At a first step, we introduce an analytical model of a piezoelectric ring responsible for energy conversion. The major deformations of the ring are considered to be the thickness deformation (Figure 2a) and the radial one (Figure 4a). Flexural modes were neglected because these are not natural deformation of the capsule. Figure 2a represents a schematic of the piezoelectric ring, the dimensions of the ring are given by its thickness $L = 1$ mm and its outer and the inner radius $r_a = 11$ mm, $r_b = 10$ mm, respectively.

Small dimensions of the piezoelectric element lead to higher resonance frequencies in comparison to those of the spherical capsule. Thus, the piezoelectric ring is used outside its resonance and the spherical shell acts as a mechanical amplifier. Our simplified model of the piezoelectric ring was based on Mason equivalent circuit theory [35], the Pz26 piezoelectric ring mechanical and electrical characteristics were taken from [36]. For each mode (thickness and radial), the ring behavior was described by an equivalent electromechanical circuit connecting the mechanical ports (forces and velocities) to the electrical port (voltage and current). This way we combined the electromechanical part with the electronics that process the energy directly in a Spice-based simulator.

2.1. Thickness Mode

2.1.1. Mason equivalent model

The piezoelectric ring in thickness resonating mode is shown in Figure 2a. Velocities v_1, v_2 and forces F_1, F_2 are parallel to the longitudinal coordinate axis Oz, A ($\simeq$ 66 mm^2) corresponds to the area of the ring. The theoretical model we have used is classical and can be found in the literature [37]. We will briefly describe it with emphasis on the essential points.

From the fundamental principle of dynamics, it can be shown that in harmonic modes, the forces (F_1, F_2) applied to the faces of the ring are related to the corresponding
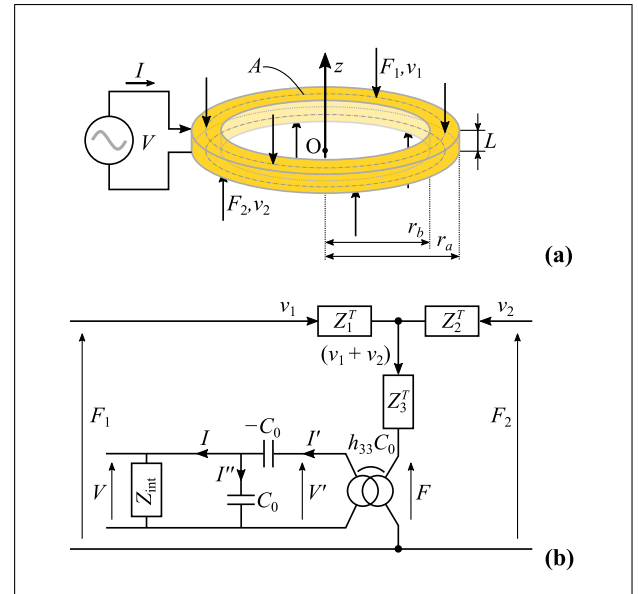

Figure 2. (a) The piezoelectric ring in thickness mode and (b) its Mason equivalent circuit.

velocities (v_1, v_2) by the expressions

$$F_1 - h_{33}e_{33}S \times A = \tag{1}$$
$$Z\left[\frac{v_1 + v_2}{\mathrm{j}\sin\sin(kl)} + \mathrm{j}\tan\tan\left(\frac{kl}{2}\right)v_1\right],$$

$$F_2 - h_{33}e_{33}S \times A = \tag{2}$$
$$Z\left[\frac{v_1 + v_2}{\mathrm{j}\sin\sin(kl)} + \mathrm{j}\tan\tan\left(\frac{kl}{2}\right)v_2\right],$$

where Z is the characteristic impedance of the piezoelectric material measured in Rayl (kg m^{-2}s^{-1}), $k = \omega\sqrt{\rho/c_{33}}$ is the wave number in m^{-1}, ρ ($= 7.70 \times 10^3$ kg/m^3) and c_{33} ($= 9.56 \times 10^{10}$ N/m^2) are respectively the density in kg/m^3 and the Young modulus. h_{33} ($= 23.7 \times 10^8$ V/m) is the charge piezoelectric constant, e_{33} ($= 14.7$ C/m^2) is the field piezoelectric constant and S is the relative deformation in z-direction.

The equivalent electromechanical circuit is shown in Figure 2b. The term $F = h_{33}e_{33}S \times A$ represents a force due to the piezoelectric contribution. The impedances are given as follows: $Z_1^T = Z_2^T = \mathrm{j}Z\tan(kl/2)$ and $Z_3^T = -\mathrm{j}Z/\sin(kl)$, the blocked capacitance $C_0 = \epsilon_{33}^s A/L$ where $\epsilon_{33}^s = 62.10^{-10}$ F/m is the clamped dielectric permittivity.

2.1.2. Resonance frequency of piezoelectric ring

Resonance frequency was determined for an unloaded ring, i.e. $F_1 = F_2 = 0$. The electrical impedance of the piezoelectric ring is then given by Equation (3) [37],

$$Z = \frac{1}{\mathrm{i}\omega C_0}\left[1 - (K_t)^2\frac{\tan(kl/2)}{(kl/2)}\right], \tag{3}$$

where $K_t = h_{33}\sqrt{\epsilon_{33}^s/c_{33}}$ is thickness coupling factor. Resonance frequency is obtained by solving Equation (3) for $Z = 0$.
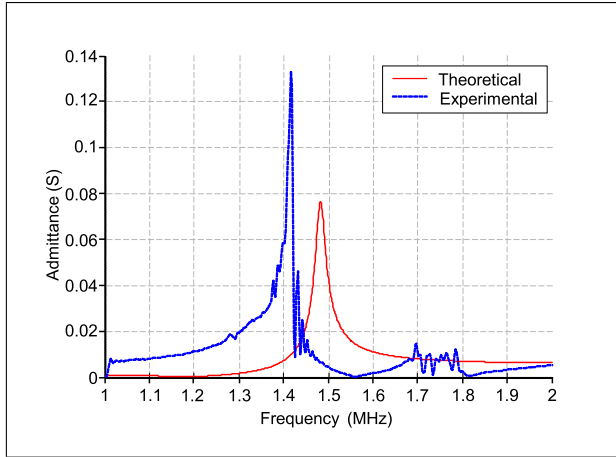
Figure 3. (Colour online) Theoretical (red solid) and experimental (blue dashed) admittances of the piezoelectric ring in thickness vibration mode.

Table I. Theoretical and measured thickness resonance frequencies (MHz) of the piezoelectric ring.

	Evan *et al.* [38]	Theoretical	Experiment
Frequency	1.7	1.48	1.42
$\Delta \times 100\%$	19.7	4.2	—

Figure 3 shows the admittance versus frequency curve of the piezoelectric ring. The resonance frequency is found to be close to 1.5 MHz. The theoretical admittance curve (see Appendix A1) is compared to the experimental curve. The experimental measurements of the admittance was done using a precision impedance analyzer (Wayne Kerr 6520).

Evan *et al.* [38] developed analytical formulas to determine the resonance frequency of a ring for various vibration modes. For the thickness mode, the resonance frequency is given by

$$f_{\text{thickness}} = \frac{1}{2L\sqrt{\rho s_{33}^D}}, \tag{4}$$

where s_{33}^D is the elastic compliance at constant charge density (see Table A1).

In Table I, theoretical and experimental values are reported and compared with the value obtained in [38]. The second line in the table shows % error for the resonance frequency $\Delta = |f_t - f_m|/f_m$ where f_t and f_m are the theoretical and measured resonance frequencies in thickness mode, respectively.

The resonance frequency predicted by the equivalent electromechanical circuit model is within the 10% tolerance of material properties provided by the manufacturer [36]. The value calculated using Equation (3) was found to be 10% off the threshold tolerance.

2.2. Radial Mode

The motion equations for radial vibrational mode [39] are written in cylindrical coordinates (r, θ, z). In Figure 4a
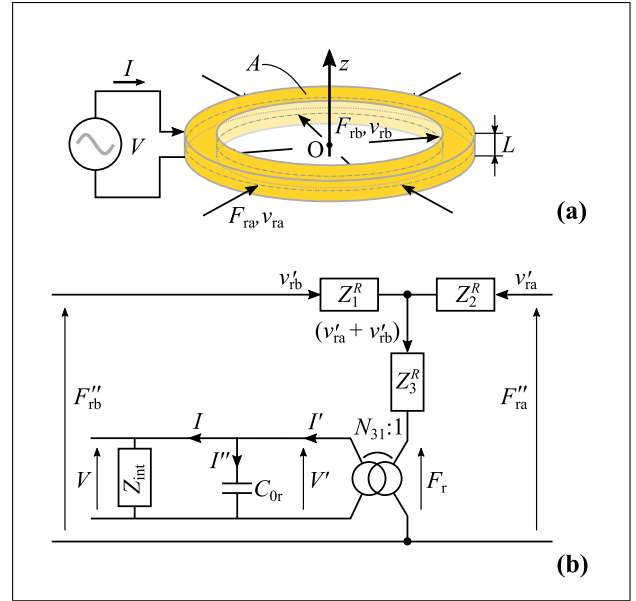

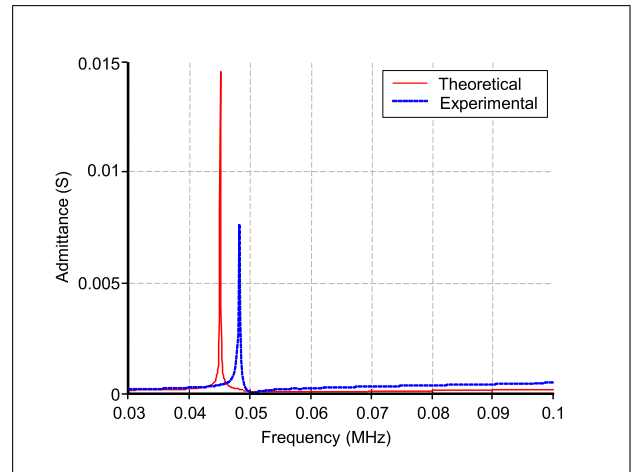Figure 4. (a) The piezoelectric ring in radial mode and (b) its equivalent electromechanical circuit.

Figure 5. Admittance of the piezoelectric ring in radial vibrational mode.

F_{ra}, F_{rb} and ϑ_{ra}, ϑ_{rb} are external radial forces and velocities at the outer and inner surfaces of the ring, respectively.

The corresponding electromechanical circuit represented in (Figure 4b) has the same structure as that representing the thickness mode but with new redefinition of the components in terms of radial parameters. For the definition of these components, see Appendix A1.

2.2.1. Resonance frequency of piezoelectric ring

The impedance function for the radial vibrational mode is presented in Appendix A2. Experimental measurement with the EIA (red solid line in Figure 5) shows that a resonance frequency is closed to 45 kHz. The theoretical curve calculated accordingly to Equation (13) is presented in the same graph (blue dashed line).

Evan *et al.* [38] proposed an approximate formula to calculate the radial resonance frequency of a piezoelectric ring,

$$f_{radial} = \frac{1}{2(r_a + r_b)\sqrt{\rho s_{11}^E}}, \qquad (5)$$

where s_{11}^E is the elastic compliance at constant electric field (see Table A1 in Appendix A1).

The comparison between the experimental and the calculated values of resonance frequencies is given in Table II. The second line in Table II shows the relative frequency prediction error $\Delta = |f_t - f_m|/f_m$ where f_t and f_m are the theoretical and measured resonance frequencies in radial mode, respectively.

The resonance frequency calculated with the electromechanical circuit model fall within the 10% tolerance guaranteed by the piezoceramics manufacturer. At the same time, Equation (5) gives the exact value of resonance frequency. We do not know if it is due to exactness of the Equation (5), or to the tolerance of PZT properties, as no statistical analysis has been done. It is worth while mentioning that the approach of Evan *et al.* [38] does not include the calculation of equivalent electrical circuit of the piezoelectric ring and thus, to determine the optimal charge impedance, which is an important goal of our present study.

3. Voltage response of the spherical transducer

3.1. Electromechanical circuits model

In the thickness vibrational mode, the electromechanical equivalent circuit (Figure 2b) is composed of two parts connected by a transformer of ratio $h_{33}C_0$. A pure mechanical part takes the forces F_1 and F_2 and velocities ϑ_1, ϑ_2 as input variables and an electric part produces the output voltage V_T and current $4I_T$ in a load Z_{int} which represents the input impedance of the harvester electronics. The voltage $\overline{V_T}$ versus the force $\overline{F_1}$ is established by applying the basic Kirchhoff's rules,

$$\overline{V_T} = \frac{2h_{33}C_0 Z_{int}}{\left(1 + jC_0\omega Z_{int}\right)\left(2h_{33}^2 C_0 Z_{elec}^T + 2Z_3^T + Z_1^T\right)}\overline{F_1}. \quad (6)$$

In this equation, Z_{elec}^T is the equivalent impedance seen by the secondary of the electromechanical transformer,

$$Z_{elec}^T = -\frac{1}{jC_0\omega} + \frac{Z_{int}}{1 + jC_0\omega \times Z_{int}}. \qquad (7)$$

In the radial vibrational mode, the voltage response is determined using the same procedure as in the thickness mode,

$$\overline{V_R} = \frac{2N_{31} Z_{int}}{\left(1+jC_{0r}\omega Z_{int}\right)\left(2N_{31}^2 Z_{elec}^R +2Z_3^R+Z_2^R\right)}\overline{F''}ra, \quad (8)$$

where $Z_{elec}^R = Z_{int}/(1 + jC_{0r}\omega Z_{int})$ is the equivalent impedance of the electrical part.

Table II. Theoretical and measured resonance frequencies (MHz) of the ring in radial mode.

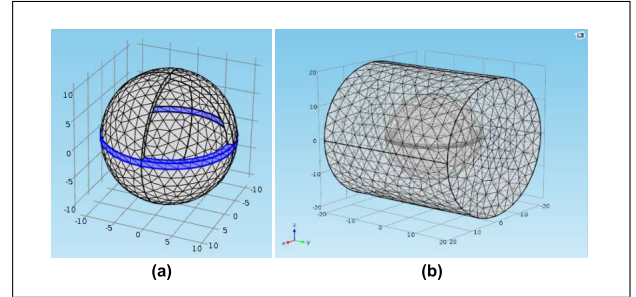|	Evan *et al.* [38]	Theoretical	Experiment
Frequency	0.048	0.045	0.048
Δ (%)	0	6.2	—

Figure 6. (a) Finite elements model of the sphere and (b) of the sphere in a fluid cavity.

3.2. Force applied on the ring and induced voltage

Deformations of the structure in aqueous media create stresses on the piezoelectric ring which are converted into electric charges. Therefore, to calculate the force field applied to the ring due to the acoustical field, a finite elements model was built with COMSOL Multiphysics (Figure 6). The model combines three physical domains: acoustics, mechanics and piezoelectricity.

Geometrical properties of the piezoelectric ring were set to be the same as for the analytical modeling (see Section 2). Two half-spheres made of PMMA (Young modulus $E = 3300$ MPa, Poisson coefficient $v = 0.39$, density $\rho = 1190$ kg/m^3) were attached to the ring from both sides. The inner radius of each semi-sphere is 10 mm (equal to the ring inner radius r_b) while their thickness is 1 mm (equal to the ring width $r_a - r_b$). The height of the semi-spherical shells was slightly reduced to take into account the ring thickness so that the whole structure formed an almost perfect spherical body.

The mesh model uses tetrahedral elements and is refined for the piezoelectric ring. The frequency range was chosen from 1 kHz to 40 kHz corresponding to the main response of the sphere. Element size was 1/4 times of the wavelength in respective constituent at the highest frequency ($\sim$ 40 kHz). The total number of degrees of freedom is 43883. It was assumed that a uniform harmonic pressure field is applied omnidirectionally on the whole surface of the sphere.

The acoustical pressure level was set to 20 kPa for each analyzed frequency, it was distributed uniformly in space. The force applied to the faces of the piezoelectric ring was obtained by integrating the pressure per unit area for each frequency. Figure 7 shows the force versus frequency curve obtained by this method. This force is used as input to the simplified Mason models of the piezoelectric ring presented above in order to determine the corresponding output voltage.
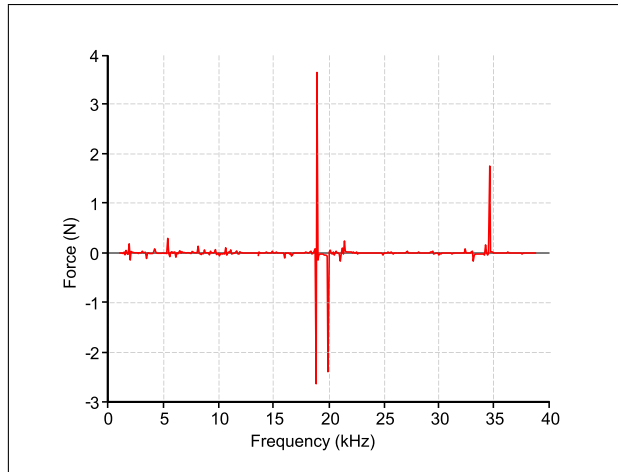
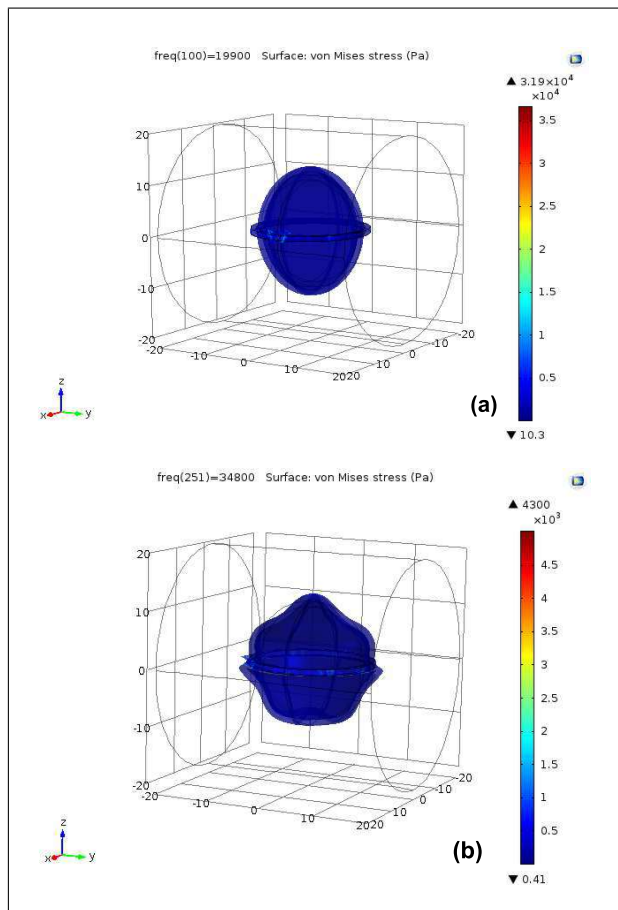Figure 7. Force applied on the ring as computed by the FEM.

Figure 8. Deformation of the sphere at two resonance frequencies (19.9 kHz (a) and 34.8 kHz (b)).

Figure 8 shows the deformation of the sphere under the action of uniform harmonic pressure field for frequencies 19.9 kHz and 34.8 kHz. The output voltage at the electrical port terminals induced by the force $F(f)$ is given by

$$V(f) = \Re e\{H(f) F(f)\}, \qquad (9)$$

where $H(f)$ is the force-voltage transfer function given by equations (6) and (8) for the thickness and the radial mode,
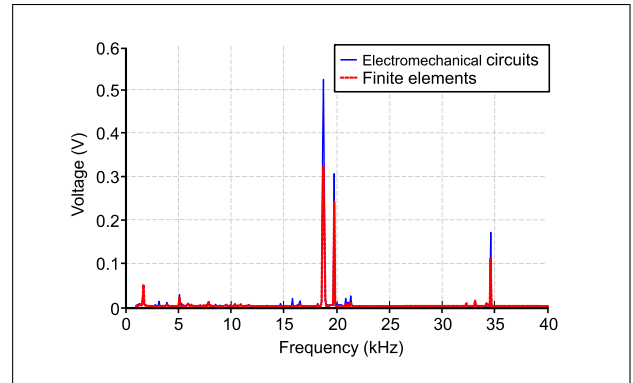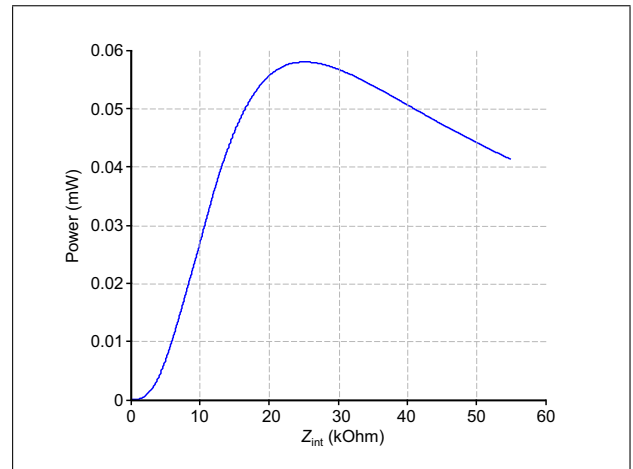

Figure 9. Total harvested voltage versus frequency computed from equivalent electromechanical circuits and finite elements.

Figure 10. Total harvested power versus load impedance Z_{int}.

respectively, $\Re e$ stands for the real part. The total voltages obtained by finite elements method and electromechanical circuits are shown in Figure 9. As one can see, the expected harvested voltage is of the order of 100 millivolts and more.

3.3. Estimation of harvested power

The two equivalent electromechanical circuits corresponding to the two vibrational modes are intended to represent the mechanical to electrical energy conversion. The electrical energy is processed by some harvesting electronics in order to supply the embedded utilities. The total load impedance is (Z_{int}) in which the electrical energy is consumed. For the sake of simplicity, Z_{int} is assumed here to be purely resistive. To consider this charge effect, the transferred power has been analytically calculated with equations (6) and (8) depending on the load impedance Z_{int}. The voltage response presented in Figure 9 was used as an input for these calculations.

The variation of the total power is shown in Figure 10, one can observe that the power reaches a maximum value of 58 µW for an optimal load impedance $Z_{\text{int}} \simeq 25 > k\Omega$. This harvested power level is sufficient to supply specially designed low power electronics and processors.

4. Experimental characterization

4.1. Frequency response and emission diagrams of the spherical transducer in air environment

The purpose of this section is experimental characterization of energy harvesting performance of the spherical shell. The sensor prototype has been realized according to the brief description given in section 2 and contained no electronics inside. It consisted of two PMMA half-spheres bonded on a piezoelectric ring at the center by a double component epoxy glue (Figure 11a). Similarly, as it was mentioned in Section 3.2, the height of the half-spheres was reduced by 0.5 mm in order to account for the ring thickness. Electrical connection with the ring was made with a thin coaxial cable. The cable was soldered to the ring inside the sphere, and the other cable's extremity was brought out from the sphere via a small hole. The hole was leak-proofed by the same epoxy glue as was used for the half-spheres assembly. All sensor dimensions correspond to those given in precedent sections: shields and ring outer radius is equal to 11 mm, and their inner radius is equal to 10 mm.

The spherical transducer frequency response was recorded with a EIA Wayne Kerr 6520 (Figure 11b) and compared to the values predicted with FEM modeling (Figure 7). As shown in Figure 11b, the electric impedance exhibits several resonance frequencies. The first two resonance modes are observed experimentally at frequencies 20.5 and 33.3 kHz while the FEM modeling predicts a response at frequencies 19.9 and 34.8 kHz. These discrepancies are most probably due to imperfections of spherical shield assembly with epoxy glue. Further characterization with a Laser Doppler Vibrometer (LDV) revealed the accuracy of resonance patterns corresponding to the first two modes (see below). Complete simulation of spherical shield behavior with FEM is out of the scope of this work. However, a relative correspondence of the results for the first two resonance modes allows validating FEM model and the estimated power output as presented in Section 3.3.

The spherical shell directivity patterns were also recorded at the main resonance frequencies using an LDV. The experimental setup is depicted in Figure 12. The spherical transducer was used in emitter mode. As the sensor's outer shell is made of transparent acrylic glass, it was necessary to cover the measurement zone with an ultrathin retro-reflective adhesive tape (Polytec A-RET-S001, Figure 12a). Taking into account a rather low measurement frequency range (1–100 kHz), such modification was not expected to modify the transducer behavior and no change in impedance curve has been observed with the EIA.

The spherical sensor was mounted on a manual rotating plate providing angular positioning in the horizontal plane perpendicular to the Oz axis (Figure 12a). In Figure 12b, the entire experimental setup for LDV characterization is presented. The LDV consisted of the Polytec OFV-552 optical fiber head connected to the Polytec OFV-5000 controller. The VD-09 velocity decoder (DC –
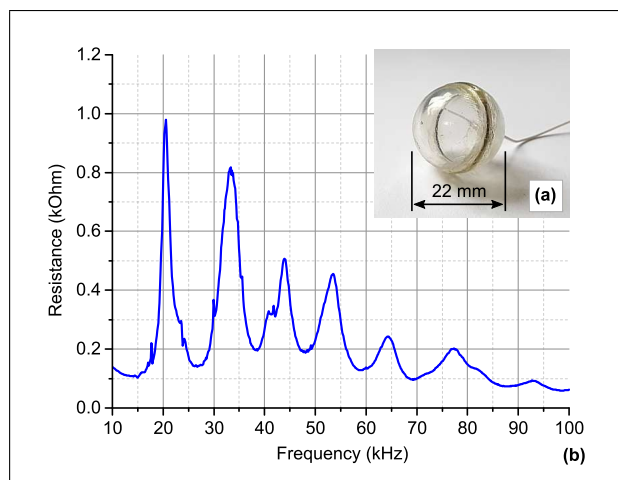

Figure 11. (a) Photo of the realized spherical transducer and (b) real part of its electrical impedance vs frequency.
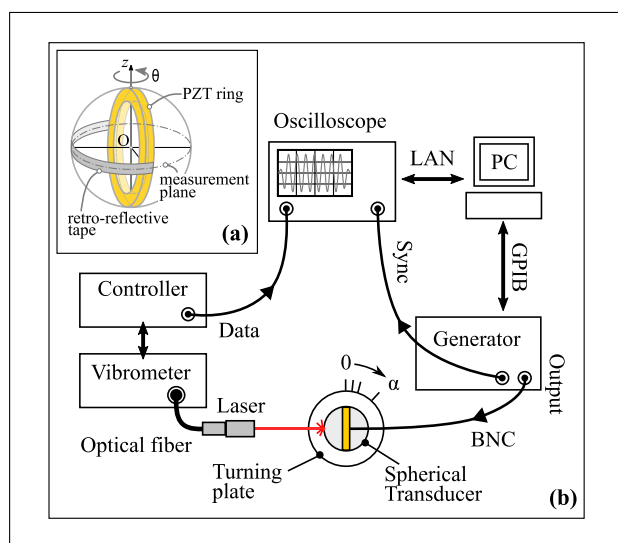

Figure 12. (a) Scheme of the spherical transducer scanning configuration with the LDV and (b) of whole experimental LDV setup.

1.5 MHz measurement range) was chosen. Decoded signal from the LDV was acquired by a digital oscilloscope (LeCroy 44Xi) and transmitted by Ethernet connection to a personal computer (PC) for further analysis. Excitation of the sensor was provided by the Agilent 33220A function generator. The generator was controlled via GPIB by the computer and the maximum output amplitude of 20 Vpp (in the "high-Z load" mode) was used.

The spherical shell directivity patterns were obtained by measurement of the normal vibrational component along a half circle in a plane perpendicular to the piezoelectric ring Figure 12a. The angle scanning range was $\theta = -90° \ldots 90°$ with the angle step $\delta\theta = 1°$. The acoustical field distribution on the opposite half circle not covered by measurement points is assumed to be identical by symmetry. Frequency sweeping from 5 to 100 kHz with the step of 0.2 kHz was performed. For each frequency, a tone burst of 7 cycles was emitted. The starting part of the signal cor-
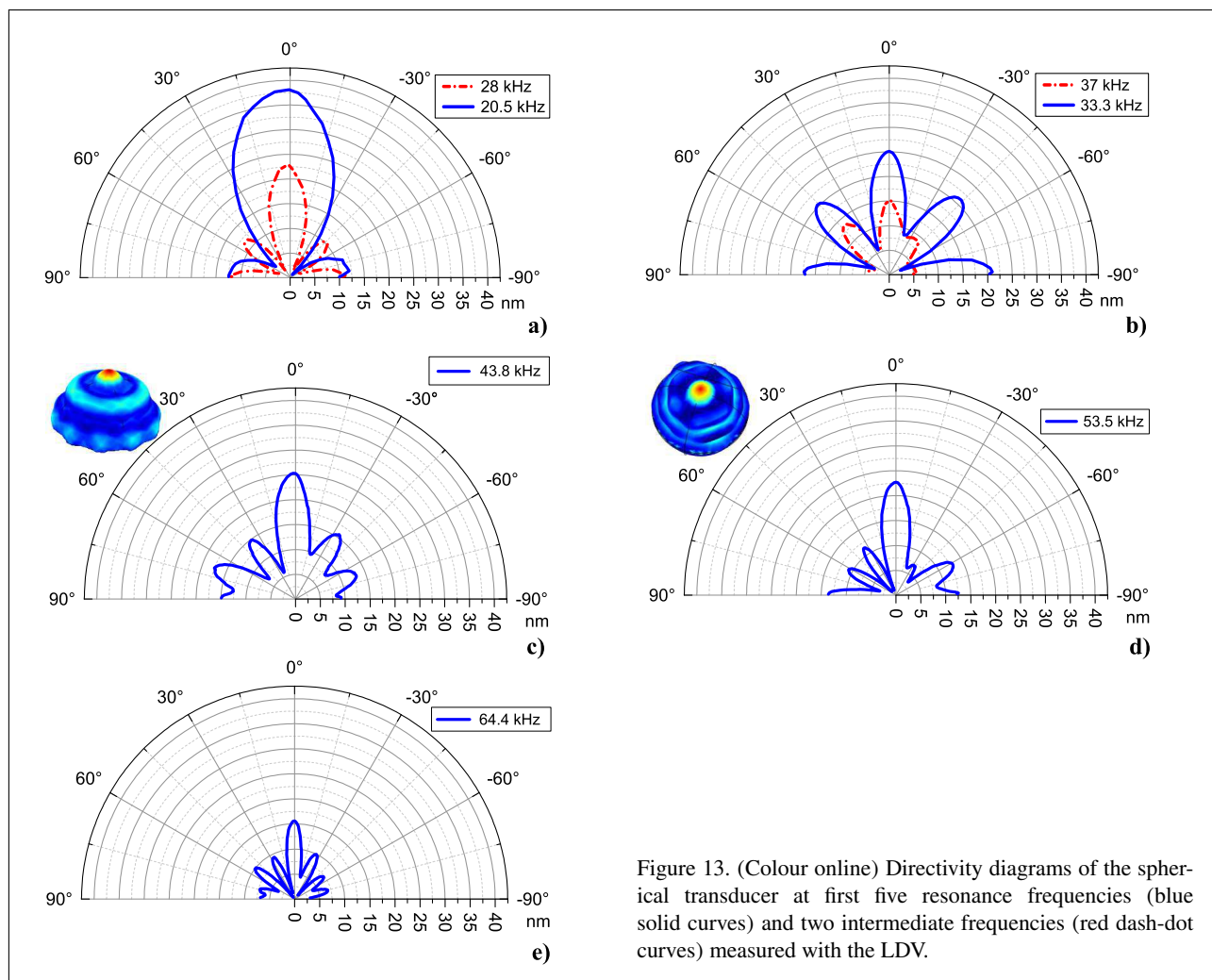
Figure 13. (Colour online) Directivity diagrams of the spherical transducer at first five resonance frequencies (blue solid curves) and two intermediate frequencies (red dash-dot curves) measured with the LDV.

responding to the first 3 cycles was omitted in order to cancel out transient effects. Only the 3 following cycles of the transducer response were analyzed using the FFT algorithm. In such a way, ending transition effect were canceled out as well.

Spherical transducer directivity patterns for the five first resonance frequencies are presented in Figure 13. These patterns correspond to magnitude of surface displacement versus emission angle characteristics. Figure 13 demonstrates that the spherical shell with rigid piezoelectric disc exhibits multi-lobe resonance patterns as in a well-studied case of a uniform spherical shell [40]. For the latter shell the fundamental mode represents 'respiratory' movements, when the shell maintains its spherical form while having its radius oscillating. For the considered case, the presence of the rigid ring in the structure makes the fundamental mode to be directive with the maximum in the direction perpendicular to the ring (Figsures 8a and 13a). Experimental measurements and FEM modelling for superior resonance frequencies reveal the presence of axisymmetric modes only. Simulated resonance pattern for the 2nd mode shown in Figure 8b corresponds to the directivity pattern in Figure 13b. The FEM-modelled resonance patterns for the 3rd and 4th resonance modes are shown in the

insets of Figures 13c and 13d respectively. Two intermediate frequencies 28 and 37 kHz (Figure 13a,b) are included as well in order to illustrate that non-negligible acoustic power is emitted out of resonances as well. Some asymmetry can be observed (especially, for 37 kHz); which is probably due to imperfections of transducer assembly.

As one can observe, the acoustical emission in the whole angle range ±90° with some nodes and antinodes (minima and maxima) is possible. Returning to the intended use of the spherical transducer under a broadband excitation in 10–100 kHz frequency range, one can expect that for each acoustic field incidence direction there will correspond some directivity lobes assuring high efficiency of energy conversion.

4.2. Directivity of the spherical receiver in water

Low directivity of acoustical sensors and harvesters is important for underwater applications as signals or energy are supposed to come from random directions. Our measurements were carried out in a tank (with $100 \times 100 \times 50$ cm dimensions) filled with water, the spherical transducer was used in receiver mode. In order to characterize the sensor in a wide frequency range, two different high power transducers were used. The first transducer is
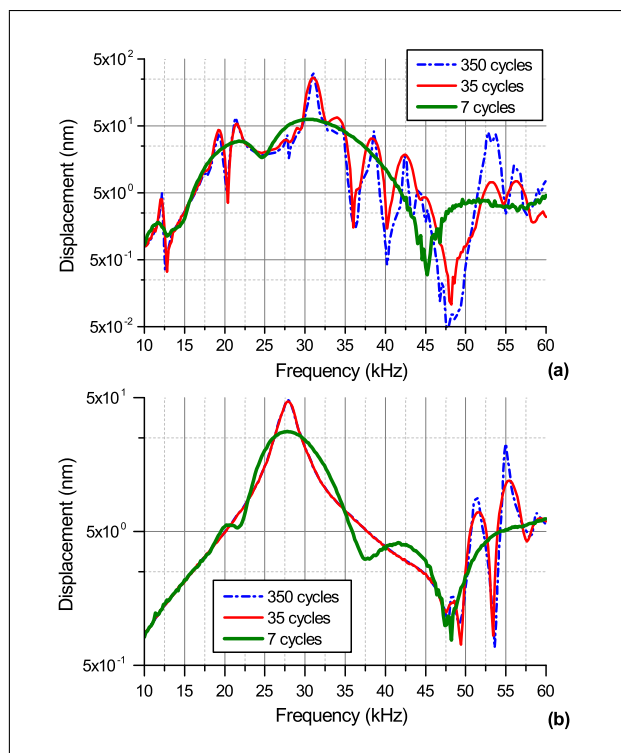
Figure 14. Frequency responses of the (a) Tonpilz and (b) the single-piezoelement transducer measured with the LDV.

a Tonpilz-type [41] one, while the second is a "classical" transducer based on a single piezoelectric element; both transducers had the same circular aperture of 40 mm diameter.

Frequency responses of the transducers was characterized with the LVD (Figure 14). The measurement point is situated in the center of the aperture. The transducers exhibit almost piston-type emission, they were excited with the Agilent 33220A generator (20 Vpp). The Tonpilz-type transducer has several resonance frequencies due to different vibrational modes while the other transducer possesses one main resonance. Emission frequencies of the both transducers were closed to resonance frequencies of the spherical shell. In order to avoid reflections from side walls of the water tank, the transducers were excited with short 7 cycles tone bursts. This permitted equally to broaden the transducers emission spectra at the expense of the output power. The situation is illustrated in Figure 14, where transducer responses for 350, 35 and 7 cycles tone burst excitation are presented.

It is known, that external or internal static pressure can provoke a shift of the spherical shell resonance frequencies [42]. We estimated this shift using the EIA and by comparing the impedance curves for the submerged spherical transducer (10 cm depth in water, red dash-dot curve in Figure 15) with the impedance curve corresponding to air environment (similar to Figure 11, blue solid curve in Figure 15). Frequency shifts starting from 8.4 kHz for the first resonance and progressing till 15.4 kHz for the fifth one were observed. For this reason, all our experiments in water were limited to 10–60 kHz frequency range.
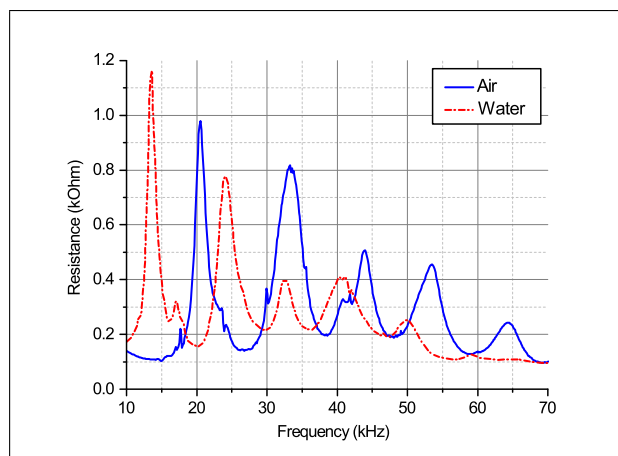

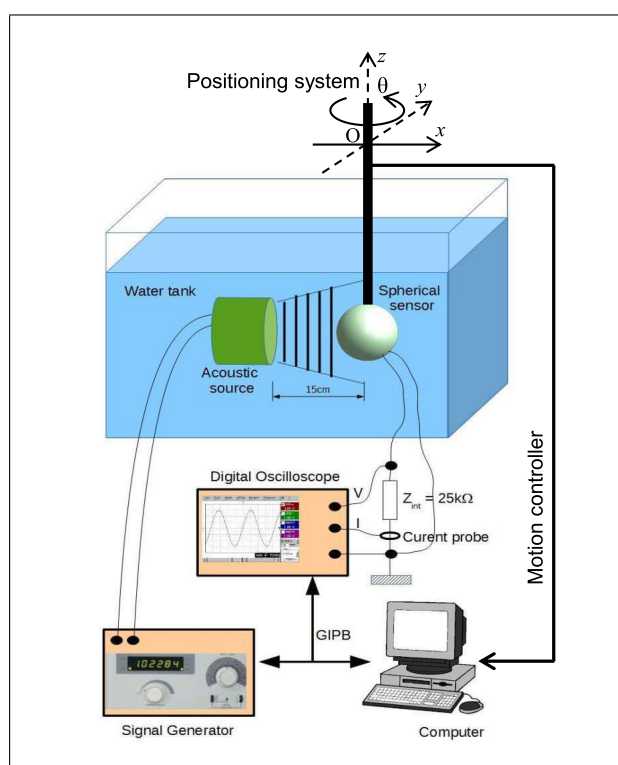Figure 15. Effect of external water pressure on impedance curve of the spherical transducer.

Figure 16. Experimental setup for underwater energy harvesting measurements.

The scheme of the setup for underwater measurements is presented in Figure 16. The spherical transducer was mounted on a 4-axis positioning system (Micro-Contrôle, 3 translation axes, and one rotational axis in the horizontal plane Oxy), the piezoelectric ring of the transducer was perpendicular to the Oxy plane. The center of the sphere situated at the central directional axis of the emitter.

The acoustical sensor was connected to a 25 kΩ charge accordingly to the calculations in Section 3.3. The sensor output was connected to a digital oscilloscope (LeCroy 44Xi) using a 1 MΩ coupling. In order to take power measurements, a current probe was connected to the oscilloscope as well. Excitation of the transducers was provided
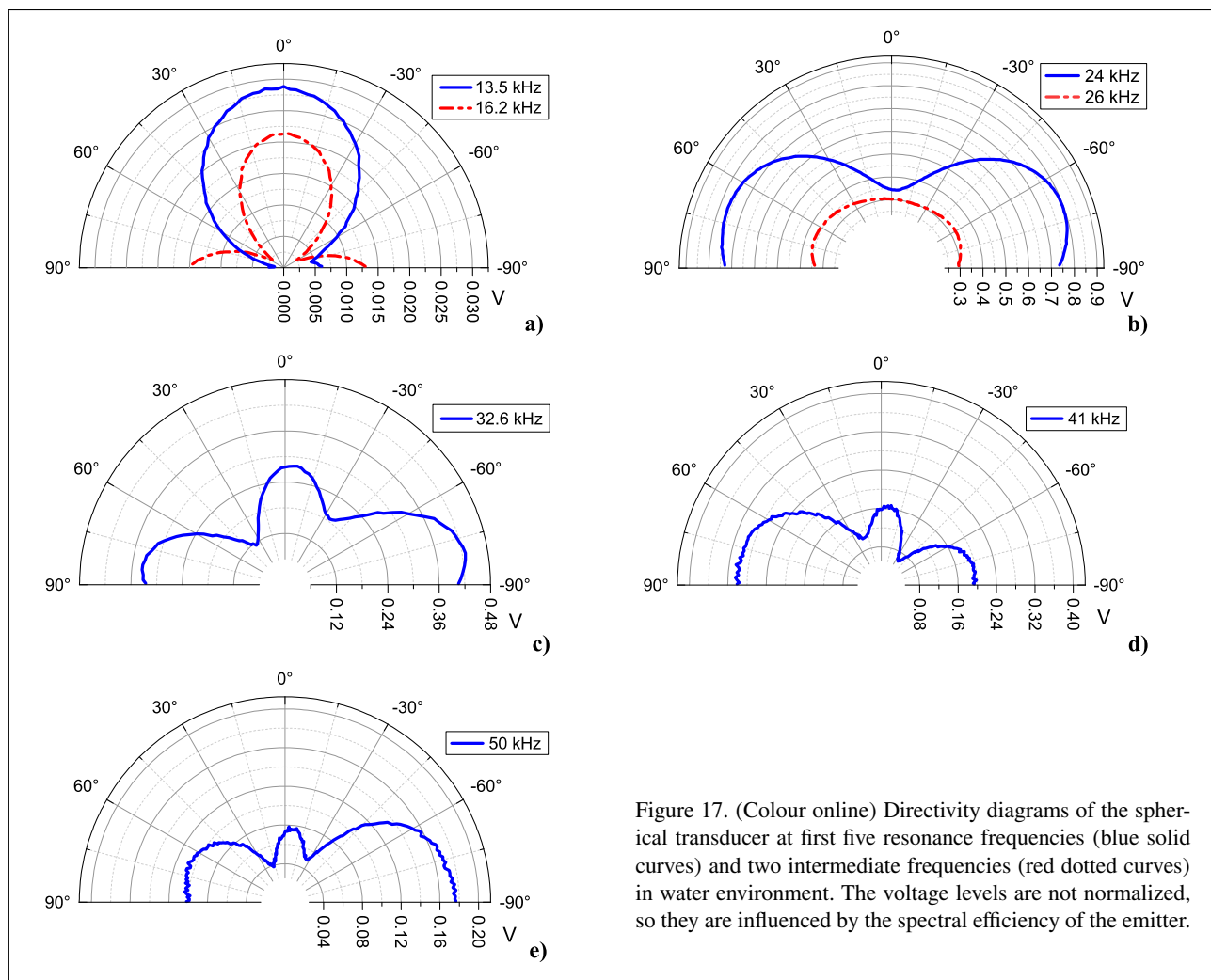
Figure 17. (Colour online) Directivity diagrams of the spherical transducer at first five resonance frequencies (blue solid curves) and two intermediate frequencies (red dotted curves) in water environment. The voltage levels are not normalized, so they are influenced by the spectral efficiency of the emitter.

by the Agilent 33220A function generator with 20 Vpp output amplitude. The positioning system was operated by a personal computer via the Newport ESP 301 motion controller.

The spherical receiver was placed at a distance of 50 cm from the emitter. For the highest frequency of 60 kHz used in this study, near or Fresnel field zone r_f is given by $r_f = D^2/4\lambda = 1.6$ cm [43]. This distance represents a demarcation between Fresnel and Fraunhofer field regions. Operation in far field Fraunhofer zone beyond 1.6 cm distance allows to neglect diffraction effects and to assume that the spherical receiver is placed under a plane wave projection. In this case, contrary to the point measurement with the LDV presented in Figure 13, several directivity lobes of the sphere are simultaneously subjected to excitation with incident acoustical field.

Similar to the case of the LDV measurements, the spherical receiver was rotated along the Oz axis (Figure 12a) in the angle scanning range $\theta = -90° \ldots 90°$ and with the angle step $\delta\theta = 1°$. The obtained reception directivity distributions for five resonance frequencies corresponding to the EIA measurements (Figure 15) as well as for two intermediate frequencies are presented in Figure 17. One can observe that these characteristics are not strictly om-

nidirectional, but there is no "dead" angle sectors, except for the case of 13.5 kHz reception exhibiting a bipolar behavior. The received voltage was not negligible at intermediate frequencies. It is interesting that at 26 kHz the spherical transducer exhibits an almost omnidirectional reception. In contrary to the results presented in Figure 13, the first resonant mode in Figure 17 shows a lower voltage response because the frequency 13.5 kHz is situated at the limit of the bandwidth of the transmitter emission spectrum (Figure 14). Therefore, the spherical transducer receives less of acoustic power at this frequency, which influences the absolute value of voltage response.

In contrast with the LDV measurements (Figure 13), the spherical receiver appears to be more efficient at $\theta = \pm 90°$ for frequencies higher than 24 kHz. This increased efficiency in the perpendicular direction is possibly due to the fact that multiple directivity lobes are excited by an incident plane wave simultaneously. Starting from the third resonance frequency at 32.6 kHz (Figure 17c), one can observe an asymmetry in reception which alternates from one resonance to another (Figure 17d and 17e). As in the case of the LDV measurement, this behavior is supposed to be the consequence of imperfections of spherical shell assembly.
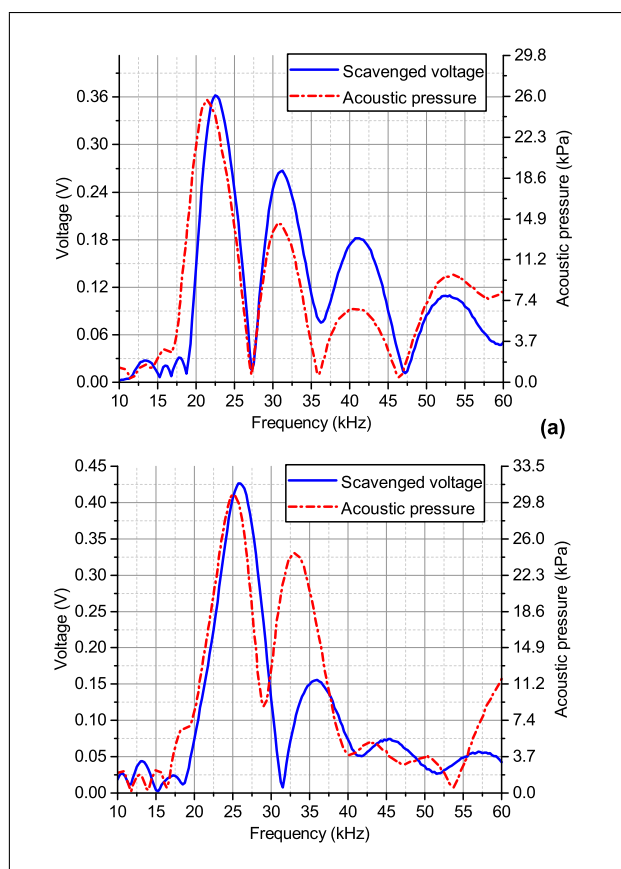
Figure 18. (Colour online) Harvested voltage for 25 kΩ load (blue solid) and acoustical pressure (red dash-dot) versus frequency for the case of incident acoustic field created by the (a) Tonpilz-type and (b) single-element transducer.

4.3. Measurement of energy harvesting performances

The experimental configuration for the studies reported below is similar to that presented in the precedent section (Figure 16). In order to quantify the efficiency of energy harvesting with the spherical transducer, electrical measurements of harvested power with the oscilloscope were combined with absolute measurements of acoustical pressure Brüel&Kjær 8103 hydrophone type. First, a measurement with the spherical receiver was performed, and then, the hydrophone was introduced at the same position of the transducer and the measurement was repeated. This permitted us to relativize the scavenged electrical voltage accordingly to acoustic pressure applied to the energy harvesting device.

Two typical curves for these combined measurements are presented in Figure 18a,b. For Figure 18a, the incident acoustical field is created by the Tonpilz-type transducer, the receivers were located at 50 cm distance from the emitter, the PZT ring was set parallel to the face of the transducer ($\theta = 0°$). Acoustic pressure at 13.5 kHz corresponding to the first resonance frequency was found to be weak, however the other four resonances could be clearly seen. Observable shift in frequency peaks between the hydrophone measurement (red dash-dot curve) and the elec-
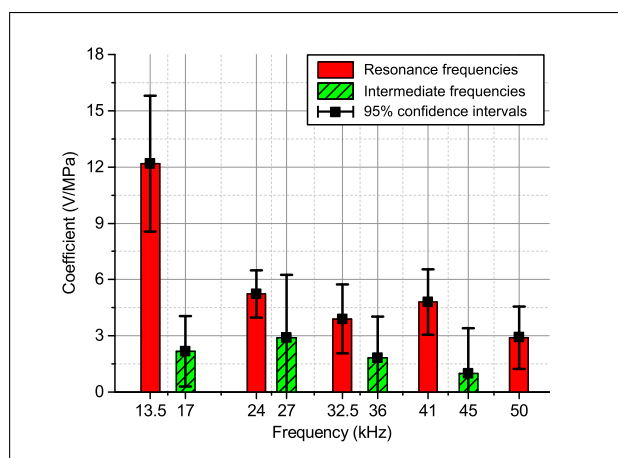

Figure 19. (Colour online) Conversion coefficient values for 5 resonance frequencies (red bars) and for several intermediate frequencies (green hatched bars).

trical measurement of the spherical transducer response (blue solid curve) is due to the fact that the resonance frequencies of the receiver and the emitter does not coincide exactly (Figure 14a vs Figure 15). Figure 18b represents the same measurements for the single-element transducer.

As one can observe in Figure 18, for an acoustic field pressure around 20 kPa, it is possible to obtain a voltage response of the order of several hundreds millivolts (for example, 360 mV for 24 kHz in Figure 18a). This corresponds to a power of several microwatts scavenged using a 25 kΩ resistive load (2.5 μW for the same measurement in Figure 18a). The single-element transducer creates a slightly higher acoustical pressure, but it has a narrower frequency band Figure 18b. The spherical transducer response exhibits the same behavior as in the precedent case. The harvested power values are slightly below the predicted values in Section 3.3 because several sources of losses were not taken into account in the models (mechanical and electrical losses, coupling between the sphere and the piezoelectric ring). However, these power levels must be sufficient to supply energy for low power electronics.

Finally, this experimental configuration permitted to measure acoustic-to-electric energy conversion coefficient (Figure 19). Measurements were taken for three emitter-receiver distances: 50, 30 and 15 cm; for three incident angles: 0°, 45° and 90°; and for two types of emitters: The Tonpilz and the single-element type transducers. Measurement error was estimated using a standard statistical procedure [44], the 95% confidence level was used. Average conversion coefficient value for 10–60 kHz range is of the order of approximately 3 V/MPa, the maximum value of 12 V/MPa is obtained for the first resonance frequency at 13.5 kHz (Which is in agreement with Figure 13, the first resonant mode showed the highest displacement response among the five vibration modes). Several coefficient values were also provided for some intermediate frequencies as well; one can see that these coefficients are not negligible and they have an average value of about 2 V/MPa.

The results presented in Figure 19 allows estimating power harvesting performance in broadband mode. For example, assuming 10 kPa uniform broadband acoustical field level, one can expect to harvest 3.32 µW due to 5 main resonance modes. This power level could be higher due to the contribution of intermediate frequencies.

5. Conclusion

An efficient, wide band and low-cost piezoelectrical energy harvester and sensing node container have been proposed for UWSNs applications. The proposed concept could be considered as three in one device: first, it is a spherical container sensing node, second the device can be used as an ambient vibrational energy harvester and third, ambient noise used for energy harvesting could be considered as a signal as well. We realized a prototype of the proposed device using a shell of 2.2 cm diameter and low-cost components directly available on the market.

Electromechanical circuit model coupled with FEM simulations showed an optimal load impedance value of 25 kΩ for energy harvesting.

The experimental measurements in air environment with EIA and LDV revealed the existence of several structural resonance modes in the range of 20–80 kHz, and these were shifted down to the range of 10–60 kHz for underwater measurements.The low directivity dependence was revealed for the underwater spherical transducer in receiver mode, expect the first resonance mode exhibiting a dipole pattern. As for power harvesting performance, our measurements showed an average conversion coefficient value of about 3 V/MPa, with a maximum value of 12 V/MPa obtained for the first resonance frequency.

5.1. Future Work

Future research efforts will be guided towards the adjustment of the dimensions of the spherical transducer to explore different ranges of frequency for the harvester operation. Miniaturizing the dimension of the sensor for possible biomedical applications, such as the detection of bioacoustics signals. In addition, we will be concentrating on the full conception and realization of the energy extraction circuit for rendering the sensor autonomy.

Appendix

A1. Redefinition of equivalent circuit components for radial vibrational mode

In the scheme of Figure 4b,

$$C_{0r} = \epsilon_{33}^T A / L \left[1 - 2d_{31}^2 / \left[\epsilon_{33}^T (s_{11}^E + s_{12}^E) \right] \right]$$

is the blocked capacitance of the ring, $N_{31} = \pi^2 \alpha r_a r_b d_{31} / (s_{11}^E + s_{12}^E)$ is the electromechanical coupling factor of the ring, s_{ij}^E is elastic compliance constants measured at constant electric field, d_{31} is piezoelectric strain constant,

Table A1. Parameters of Pz26 piezoceramics used for analytical calculations and FEM simulation.

Parameter	Value
$\epsilon_0 (F/m)$	8.85×10^{-12}
$\epsilon_{33}^s / \epsilon_0$	700
$\epsilon_{33}^T / \epsilon_0$	1300
$\rho (kg/m^3)$	770
$h_{33} (V/m)$	23.7×10^8
$e_{33} (C/m^2)$	14.7
$d_{31} (C/N)$	-130×10^{-12}
$c_{33}^D (N/m^2)$	9.56×10^{10}
$c_{11}^E (N/m^2)$	7.7×10^{10}
$s_{33}^D (m^2/N)$	11×10^{-12}
$s_{11}^E (m^2/N)$	13×10^{-12}
$s_{12}^E (m^2/N)$	-4.35×10^{-12}

ϵ_{33}^T is dielectric constant measured at constant stress, $A = \pi(r_a^2 - r_b^2)$ is the cross-sectional area, $\alpha = \omega/v_r$ is the radial wave number, $v_r = \left(c_{11}^E\right)^{1/2}/\rho$ is the sound velocity, $c_{11}^E = 1/[s_{11}^E(v_{12}^2)]$ and $v_{12} = -s_{12}^E/s_{11}^E$ is the Poisson ratio. Numerical values of these variables can be found in Table A1.

Forces and velocities are given by: $F_{ra}'' = (\pi \alpha r_b/2)F_{ra}$, $F_{rb}'' = (\pi \alpha r_a/2)F_{rb}$, $v_{ra}' = 2v_{ra}/(\pi \alpha r_b)$, $v_{rb}' = 2v_{rb}/(\pi \alpha r_a)$ and $F_r = N_{31}V$, with $V = E_z L$, with E_z the electric field in the z-direction.

The expressions for the three impedances Z_1^R, Z_2^R, Z_3^R are given by

$$Z_1^R = \frac{\pi^2 (\alpha r_a)^2 Z_{rb}}{4j} \left[\frac{Y_1(\alpha r_a)J_0(\alpha r_b) - J_1(\alpha r_a)Y_0(\alpha r_b)}{J_1(\alpha r_a)Y_1(\alpha r_b) - J_1(\alpha r_b)Y_1(\alpha r_1)} \right.$$
$$\left. + \frac{(1 - v_{12})}{\alpha r_b} \right] \tag{A1}$$
$$- j\frac{\pi \alpha r_a Z_{rb}}{2} \frac{1}{J_1(\alpha r_a)Y_1(\alpha r_b) - J_1(\alpha r_b)Y_1(\alpha r_a)},$$

$$Z_2^R = \frac{\pi^2 (\alpha r_b)^2 Z_{ra}}{4j} \left[\frac{Y_1(\alpha r_b)J_0(\alpha r_a) - J_1(\alpha r_b)Y_0(\alpha r_a)}{J_1(\alpha r_a)Y_1(\alpha r_b) - J_1(\alpha r_b)Y_1(\alpha r_1)} \right.$$
$$\left. - \frac{(1 - v_{12})}{\alpha r_a} \right] \tag{A2}$$
$$- j\frac{\pi \alpha r_b Z_{ra}}{2} \frac{1}{J_1(\alpha r_a)Y_1(\alpha r_b) - J_1(\alpha r_b)Y_1(\alpha r_a)},$$

$$Z_3^R = j\frac{\pi \alpha r_a Z_{rb}}{2} \frac{1}{J_1(\alpha r_a)Y_1(\alpha r_b) - J_1(\alpha r_b)Y_1(\alpha r_a)}$$
$$= j\frac{\pi \alpha r_b Z_{ra}}{2} \frac{1}{J_1(\alpha r_a)Y_1(\alpha r_b) - J_1(\alpha r_b)Y_1(\alpha r_a)}. \tag{A3}$$

In these equations, J_0, Y_0, and J_1, Y_1 are the Bessel functions of zero and first order respectively, $Z_{ra} = \rho v_r S_a$, $Z_{rb} = \rho v_r S_b$, with $S_a = 2\pi r_a L$ and $S_b = 2\pi r_b L$ the outer and inner surfaces of the ring respectively. Refer to Table A1 for the numerical values of introduced variables.

A2. Resonance frequency calculation for radial vibrational mode

As for the thickness mode, the electrical admittance of the piezoelectric ring in radial vibration can be determined when the inner and outer faces of the piezoelectric ring are free from external constraints, i.e. $F_{ra} = F_{rb} = 0$. It is given by the expression [39]

$$Y = \frac{j\omega\epsilon_{33}^T s}{L}\left[1 - K_\rho^2 + K_\rho^2\frac{2}{r_a^2 - r_b^2}\right] \quad (A4)$$

$$\cdot \left[\frac{\left(r_a J_1(\alpha r_a) - b J_1(\alpha r_b)\right)\left(Y(r_b) - Y(r_a)\right)}{J(r_a)Y(r_b) - J(r_b)Y(r_a)}\right.$$

$$\left. + \frac{\left(r_a Y_1(\alpha r_a) - r_b Y_1(\alpha r_b)\right)\left(J(r_a) - J(r_b)\right)}{J(r_a)Y(r_b) - J(r_b)Y(r_a)}\right],$$

where $K_\rho^2 = 2d_{31}^2/(\epsilon_{33}^T(s_{11}^E + s_{12}^E))$ is the electro-mechanical coupling factor, J_0, Y_0, and J_1, Y_1 are the Bessel functions of zero and first order respectively, $J(x), Y(x)$ are two functions given by

$$J(x) = \frac{-\alpha J_2(\alpha x)(1 - v_{12})}{1 + v_{12}} + \alpha J_0(\alpha x), \quad (A5)$$

$$Y(x) = \frac{-\alpha Y_2(\alpha x)(1 - v_{12})}{1 + v_{12}} + \alpha Y_0(\alpha x). \quad (A6)$$

The resonance frequency is obtained when the electric admittance tends to infinity which corresponds to

$$J(r_a)\, Y(r_b) - J(r_b)\, Y(r_a) = 0. \quad (A7)$$

References

[1] J. Wiley, his Sons: Wireless underwater sensor networks. Wirel. Sens. Netw. (2010) 399–442.

[2] N. Goyal, M. Dave, A. K. Verma: Data aggregation in underwater wireless sensor network: Recent approaches and issues. Journal of King Saud University-Computer and Information Sciences (2017).

[3] M. R. Jafri, M. M. Sandhu, K. Latif, Z. A. Khan, A. U. H. Yasar, N. Javaid: Towards delay-sensitive routing in underwater wireless sensor networks. Procedia Computer Science **37** (2014) 228–235.

[4] F. K. Shaikh, S. Zeadally: Energy harvesting in wireless sensor networks: A comprehensive review. Renewable and Sustainable Energy Reviews **55** (2016) 1041–1054.

[5] D. Ye, D. Gong, W. Wang: Application of wireless sensor networks in environmental monitoring. Power Electronics and Intelligent Transportation System (PEITS), 2009 2nd International Conference on, 2009, IEEE, 205–208.

[6] I. F. Akyildiz, D. Pompili, T. Melodia: Underwater acoustic sensor networks: research challenges. Ad hoc networks **3** (2005) 257–279.

[7] A. Davis, H. Chang: Underwater wireless sensor networks. 2012 Oceans (2012) 1–5.

[8] S. El-Rabaie, D. Nabil, R. Mahmoud, M. A. Alsharqawy: Underwater wireless sensor networks (uwsn), architecture, routing protocols, simulation and modeling tools, localization, security issues and some novel trends. Networking and Communication Engineering **7** (2015) 335–354.

[9] H. Karimi, O. Medhati, H. Zabolzadeh, A. Eftekhari, F. Rezaei, S. B. Dehno, et al.: Implementing a reliable, fault tolerance and secure framework in the wireless sensor-actuator networks for events reporting. Procedia Computer Science **73** (2015) 384–394.

[10] P. R. W. A. Kuperman: Underwater acoustics. Springer Handb (2007) 149.

[11] J. Wang, W. Shi, L. Xu, L. Zhou, Q. Niu, et al.: Design of optical-acoustic hybrid underwater wireless sensor network. Journal of Network and Computer Applications **92** (2017) 59–67.

[12] J. M. R. S. Roundy, P. K. Wright: Energy scavenging for wireless sensor networks. Springer US (2004).

[13] B. S. S. Neha, P. Mathews, V. P. Harigovindan: Multi-source energy harvesting system for underwater wireless sensor networks. Procedia Comput. Sci. (2015).

[14] D. A. Mann, D. M. Higgs, W. N. Tavolga, M. J. Souza, A. N. Popper: Ultrasound detection by clupeiform fishes. The Journal of the Acoustical Society of America **109** (2001) 3048–3054.

[15] M. Stojanovic: Underwater acoustic communications: Design considerations on the physical layer. Wireless on Demand Network Systems and Services, 2008. WONS 2008. Fifth Annual Conference on, 2008, IEEE, 1–10.

[16] P. Naughton, P. Roux, R. Yeakle, C. Schurgers, R. Kastner, J. S. Jaffe, P. L. Roberts: Ambient noise correlations on a mobile, deformable array. The Journal of the Acoustical Society of America **140** (2016) 4260–4270.

[17] Y. Xi, J. Wang, Y. Zi, X. Li, C. Han, X. Cao, C. Hu, Z. Wang: High efficient harvesting of underwater ultrasonic wave energy by triboelectric nanogenerator. Nano energy **38** (2017) 101–108.

[18] N. Z. Zenia, M. Aseeri, M. R. Ahmed, Z. I. Chowdhury, M. S. Kaiser: Energy-efficiency and reliability in mac and routing protocols for underwater wireless sensor network: A survey. Journal of Network and Computer Applications **71** (2016) 72–85.

[19] P. Glynne-Jones, M. J. Tudor, S. P. Beeby, N. M. White: An electromagnetic, vibration-powered generator for intelligent sensor systems. Sensors and Actuators A: Physical **110** (2004) 344–349.

[20] P. D. Mitcheson, P. Miao, B. H. Stark, E. Yeatman, A. Holmes, T. Green: Mems electrostatic micropower generator for low frequency operation. Sensors and Actuators A: Physical **115** (2004) 523–529.

[21] S. Roundy, P. K. Wright: A piezoelectric vibration based generator for wireless electronics. Smart Materials and structures **13** (2004) 1131.

[22] Z. L. Wang, J. Song: Piezoelectric nanogenerators based on zinc oxide nanowire arrays. Science **312** (2006) 242–246.

[23] R. Ahmed, F. Mir, S. Banerjee: A review on energy harvesting approaches for renewable energies from ambient vibrations and acoustic waves using piezoelectricity. Smart Materials and Structures **26** (2017) 085031.

[24] A. Toprak, O. Tigli: Piezoelectric energy harvesting: State-of-the-art and challenges. Applied Physics Reviews **1** (2014) 031104.

[25] S. Kim, W. W. Clark, Q.-M. Wang: Piezoelectric energy harvesting with a clamped circular plate: analysis. Journal of intelligent material systems and structures **16** (2005) 847–854.

[26] H. Sayyaadi, F. Rahnama, M. A. A. Farsangi: Energy harvesting via shallow cylindrical and spherical piezoelectric panels using higher order shear deformation theory. Composite Structures **147** (2016) 155–167.

[27] S. Kim, W. W. Clark, Q.-M. Wang: Piezoelectric energy harvesting with a clamped circular plate: Experimental study. Journal of intelligent material systems and structures **16** (2005) 855–863.

[28] S. Gonella, A. C. To, W. K. Liu: Interplay between phononic bandgaps and piezoelectric microstructures for energy harvesting. Journal of the Mechanics and Physics of Solids **57** (2009) 621–633.

[29] H. Hu, Y. Zheng, S. Jiang, Y. Hu, V. Laude: Piezoelectric harvester scavenges energy from cavity of phononic crystal. Frequency and Time Forum and IEEE International Frequency Control Symposium (EFTF/IFC), 2017 Joint Conference of the European, 2017, IEEE, 660–661.

[30] R. Ahmed, D. Madisetti, S. Banerjee: A sub-wavelength scale acoustoelastic sonic crystal for harvesting energies at very low frequencies (< 1 khz) using controlled geometric configurations. Journal of Intelligent Material Systems and Structures **28** (2017) 381–391.

[31] S. Adhikari, M. I. Friswell, D. J. Inman: Piezoelectric energy harvesting from broadband random vibrations. Smart Materials and Structures **18** (2009) 115005.

[32] C. B. Williams, R. B. Yates: Analysis of a micro-electric generator for microsystems. sensors and actuators A: Physical **52** (1996) 8–11.

[33] M. Lallart, D. Guyomar, C. Richard, L. Petit: Nonlinear optimization of acoustic energy harvesting using piezoelectric devices. The Journal of the Acoustical Society of America **128** (2010) 2739–2748.

[34] S. P. B. D. Zhu, M. J. Tudor: Strategies for increasing the operating frequency range of vibration energy harvesters: a review. Meas. Sci. Technol. **21** (2010).

[35] B. A. Auld: Acoustic fields and waves in solids. R.E. Krieger, Malabar, Florida (1973).

[36] Meggitt sensing systems, material data for ferroperm piezoceramics (based on typical values), https://www.meggittferroperm.com/wp-content/uploads/2017/10/material-properties-2011.pdf. 2011.

[37] H. T. S. Lin: Study on the sandwich piezoelectric ceramic ultrasonic transducer in thickness vibration. Smart Mater. Struct. **17** (2008).

[38] M. Evan, K. John, N. George, M. Stephen, K. James: Determination of resonant frequency of a piezoelectric ring for generation of ultrasonic waves. Innov. Syst. Des. Eng. **2** (2011) 103–110.

[39] S. Lin: Electro-mechanical equivalent circuit of a piezoelectric ceramic thin circular ring in radial vibration. Sens. Actuators Phys. **2** (2007) 505–512.

[40] W. E. Baker: Axisymmetric modes of vibration of thin spherical shell. J. Acoust. Soc. Am. **33** (1961) 1749–1758.

[41] J. N. Decarpigny, J. C. Debus, B. Tocquet, D. Boucher: In air analysis of piezoelectric tonpilz transducers in a wide frequency band using a mixed finite element-plane wave method. J. Acoust. Soc. Am. **78** (1985) 1499–1507.

[42] R. T. A. A. Piacsek, S. Abdul-Wahid: Resonance frequencies of a spherical aluminum shell subject to static internal pressure. J. Acoust. Soc. Am. **131** (2012) 506–512.

[43] G. S. Kino: Acoustic waves: devices, imaging, and analog signal processing. Prentice-Hall [u.a.], Englewood Cliffs (1987).

[44] J. M. J. S. B. Vardeman: Statistics and measurement. Stat. Methods Qual. Assur., Springer New York, New York, NY (2016) 33–105.